High-voltage pulse generator for time-of-flight mass spectrometry in electrospray thrusters

D. Villegas-Prados[a] and F.J. Blázquez-Plaza
Universidad Carlos III de Madrid, Av. de la Universidad, 30, Leganés, 28911, Madrid, Spain

(*Electronic mail: 100329613@alumnos.uc3m.es)

(Dated: 15 July 2024)

Electrospray thrusters exhibit diverse operational modes based on the nature of ejected particles. Time-of-flight mass spectrometry is frequently employed to analyze the composition of the plume. This study introduces a novel converter-based bipolar high-voltage pulse generator aimed at producing synchronized bipolar high-voltage pulses with controllable voltage levels and frequencies, specifically tailored for the study of electrospray thrusters. The proposed topology generates bipolar high-voltage rails from a low-voltage power source through the Forward-Flyback with Cockcroft-Walton voltage multiplier topology. Subsequently, fast high-voltage MOSFETs are employed to generate the high-voltage pulses. The paper outlines the operational principles and design methodologies of the pulse generator. Experimental verification corroborate its operational principles and functionalities, revealing that the pulse rise and fall times consistently remain below 30ns while the voltage can be tuned within the range of 300-1000V. An electrospray thruster was employed to conduct a thorough and practical validation of the high-voltage pulse generator. This included generating time-of-flight curves and mass spectra of the plume, resulting in precise differentiation of all particles present.

I. INTRODUCTION

A high-voltage pulse generator (HVPG) was custom-designed and constructed to facilitate precise time-of-flight (ToF) measurements of ion beams extracted from an ionic liquid electrospray thruster. In the domain of electric propulsion, an electrospray thruster functions by extracting and accelerating ions from an electrified ionic liquid propellant. Ionic liquids are electrically conductive salts in liquid state at room temperature composed of negatively and positively charged molecules. They are characterized by its low vapor pressure and stability making them ideal for space propulsion applications. The ionic liquid employed is the commonly used 1-ethyl-3-methylimidazolium tetrafluoroborate (EMI–BF_4)[1], where EMI^+ represents the cation and BF_4 the anion. Moreover, the ability to eject both positive and negative particles allows to achieve a neutral plume avoiding charge accumulation[2].

Consisting of two passive components, namely the emitter and the extractor, the electrospray thruster relies on the emitter's specialized geometric attributes, which facilitates, upon the application of high voltage to the ionic liquid, the attainment of a sufficiently electric field for the ionic liquid to deform into what is commonly referred to as Taylor cones[3]. Subsequently, particles are extracted from these cones and accelerated using the same electric field. The polarity bias between the ionic liquid and the extractor dictates whether positive or negative particles are extracted. An schematic of a single emitter electrospray thruster is shown in Fig.1.

The complexity of the electrospray thruster plume, characterized by its diverse species and varied energy distributions, poses a significant challenge to achieving optimal propulsive performance. Hence, comprehending the composition of the ion beam is key for the development and improvement of these systems. The utilization of a time-of-flight mass spectrometer (ToF-MS) stands out as the primary diagnostic tool to achieve said task and has been widely employed to characterize these devices[4–6]. By understanding the plume composition, performance parameters such as thrust, specific impulse or propulsive efficiency can be indirectly measured.

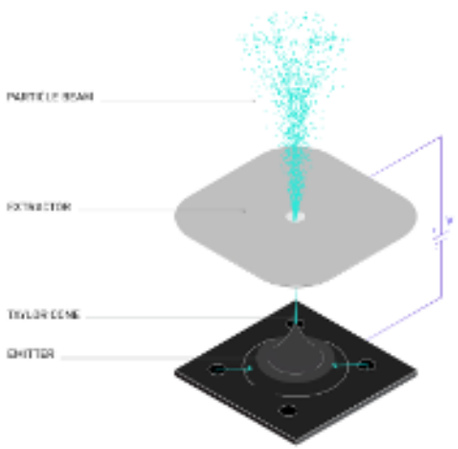

FIG. 1: Schematic of an externally wetted electrospray source, where the ionic liquid propellant flows over the emitter surface and the emitter present cone-like protrusion to enhance ion evaporation.

A critical component of ToF-MS for electrospray is the generation of a high voltage pulse. This study introduces a converter-based bipolar HVPG capable of producing synchronized bipolar HV pulses with adjustable voltage levels and frequencies. While HVPG have found applications in var-

[a]Corresponding author

ious fields such as electron-impact ionization[7], ion trap[8] or single reflection[9], there has not been a pulse generator specifically tailored for electrospray thruster applications. Section II presents the theory in ToF-MS for electrospray and requirements imposed to the HVPG. Section III explains the design of the converter-based bipolar HVPG, comprising the HV DC/DC converter, the bipolar kilovolt pulser for modulating the HV-DC outputs, and the pulse logic to achieve synchronized pulse generation. Experimental results validating the HVPG operation are provided in Section IV. Finally, Section V summarizes the conclusions of the study.

II. TIME-OF-FLIGHT MASS SPECTROMETRY IN ELECTROSPRAY

In electrospray, ToF-MS allows the identification of the different emitted particles and their contribution to the total emitted current. This is achieved by obtaining the specific charge or charge-to-mass ratio, q/m, of the particles. Because the particles emitted by the thruster have some charge q_i, they are accelerated by the potential drop V_a between the emitter and extractor. Energy conservation yields an expression for the velocity, v_i, of a particle leaving the thruster:

$$v_i = \sqrt{2\,(q/m)_i V_a} \tag{1}$$

which is dependent on the aforementioned charge-to-mass ratio, $(q/m)_i$. The beam of the thruster will consists of particles with different charges and masses. An electrospray thruster can emit two types of particles: ions, which distribution of specific charge is discrete, and droplet whose range of specific charges is a continuum. In the case of ions, these particles sometimes are emitted associated to neutral particles, forming oligomers with different degrees of solvation, n, depending on the amount of neutral attached to the ion. Typically, oligomers with $n = 0, 1, 2$ show notable current fractions, while those with higher n are often undetectable. This equation represents a simplified model that assumes the electrospray operates in a pure ionic regime without fragmentation. Despite its simplicity, it provides a useful quick estimation for calculating ion velocity and performing an initial sizing of the ToF gate.

The ToF-MS provides the mass distribution of the ion beam by measuring the ion beam current as a function of time. The particles are emitted through a section of known flight-length, L_{ToF}, resulting in a travel time, $t_i = L_{\mathrm{ToF}}/v_i$. Particles with higher q/m will arrive earlier to the collector, while those with lower q/m will arrive later in time.

A typical ToF setup for electrospray thruster characterization contains two components: an electrostatic shutter gate (ESG) and a collector, as illustrated in Fig.2. The ESG is driven by the square pulse of the developed HVPG. When the ESG is turned off, all incoming particles are able to pass. By activating the ESG on for a short time τ_{ON} ($\sim 500\ \mu$s) all particles arriving the gate are blocked. However, particles downstream of the ESG will still arrive at the collector. Since the particles have different velocities (due to different specific charges) they will hit the collector at different times, arriving first the ones with higher velocities. The collector is connected to ground through a high bandwidth and amplitude trans-impedance amplifier at the end of the flight region. Through this method, the current composition time-wave can be obtained, which later can be translated into a mass spectrum.

Moreover, a secondary electron repeller is positioned in front of the collector. The repeller consists of a grounded grid and a grid biased negatively by a few tenths of a volt. The use of the repeller allows to collect the secondary electrons generated by the impact of high-speed ions on the collector.

A. Time-of-fight electrostatic shutter gate potential

The gate design can take a variety of forms including: stopping gate, deflection gate, or Bradbury-Nielsen gate. Stopping gates consists of semi-transparent grids spaced by a few millimeters. By biasing the middle grid to a voltage larger than the source potential all the ions are stopped. The main drawback is erosion of the thruster surface since particles are reflected back when the gate is active. The deflection gate approach is a simpler and more reliable alternative. It consists of a perpendicular electric field (to the ion beam) created by means of two biased plates, eliminating the needs of grid which reduce the current and avoiding the generation of SEE. Bradbury-Nielsen gates are formed of interleaved wires, increasing the transparency and reducing erosion and backstreamed particles, but present challenges due to its complex manufacturing[10].

In this work, the ESG developed is a deflection gate, due to its easy manufacturing, implementation and reduced erosion. By applying a bias to the gate, particles are deflected, preventing them from reaching the collector. The deflection angle, θ_d, experienced by an ion passing through the activated electric field is governed by

$$\theta_d = \arctan\left(\frac{t_g}{4s_g}\frac{V_g}{V_a}\right) \tag{2}$$

where t_g is the thickness of the gate plates, s_g the spacing of the plates, and V_g the differential voltage between gate electrodes. For proper design of the ESG, θ_d must exceed the collection angle, θ_c, which is the maximum angle deviation a particle can have to reach the collector while the gate is deactivated. This relationship is encapsulated by the trigonometric expression

$$\theta_c = \arctan\left(r_c/L_{\mathrm{ToF}}\right) \tag{3}$$

where r_c denotes the radius of the collector. Solving the inequality $\theta_d > \theta_c$ yields a constraint on the differential voltage supplied to the pulse generator, expressed as:

$$V_g > \frac{4s_g r_c}{t_g L_{\mathrm{ToF}}} V_a \tag{4}$$

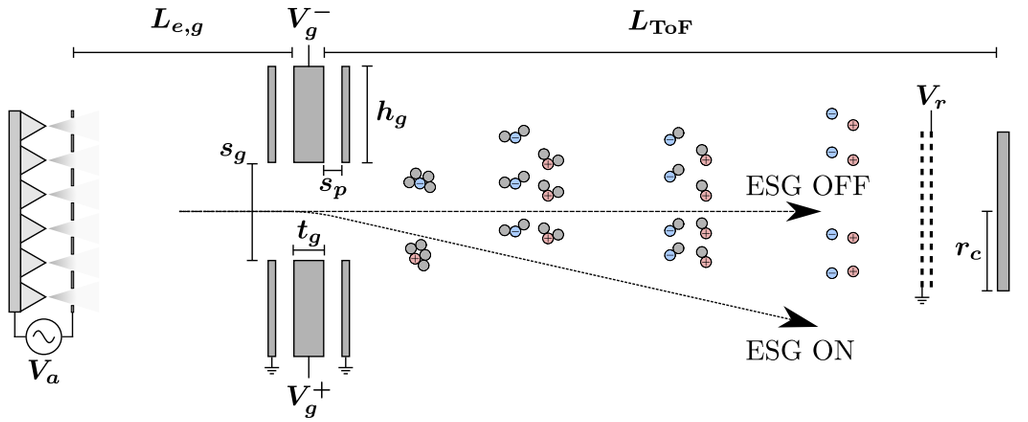

FIG. 2: Schematic of time-of-flight setup with a deflection gate as electrostatic gate shutter. When the ESG is in OFF state particles are able to reach the collector, while when the state is ON, particles are deflected, hence not collected.

While numerous combinations may satisfy this condition, the primary constraint often lies in the flight length, dictated by the capabilities of the vacuum facility. Given that the gate geometry (s_g, t_g) closely matches the thruster dimensions ($\sim$10 mm), and considering a maximum operating voltage of the electrospray thruster used in for this analysis, $V_a = 2$ kV, the minimum operating voltage of the high-voltage pulse generator is determined by the vacuum facility. Reducing the flight length is advantageous as more current can be collected reducing noise levels. However, as discussed in Sec.II B, higher resolution times are needed. The developed pulse generator is capable of supplying up to +1 kV and -1 kV to the plates resulting in a gate voltage, $V_g = 2$ kV. A preliminary numerical analysis considering $t_g = 5$ mm, $s_g = 12$ mm, $r_c = 45$ mm, shows that with that selected V_g, L_{ToF} can be reduced to 432 mm.

This analysis serves as a basis for selecting the operating voltage of the gate, depending on the characteristics or requirements of the facility. Longer flight lengths necessitate a lower gate voltage. However, we selected a desired deflection angle that is at least 1.5 times greater than the collection angle to incorporate a safety factor. This precaution accounts for the fact that our analysis does not consider potential fragmentation or ion evaporation from droplets, which would increase the m/q ratio and result in lower deflection angles[11]. Accounting for this safety margin upholds the reliability and efficacy of the electrostatic shutter gate. The vacuum facility for this study allows for setting a flight length of 700 mm which results in $\theta_c = 3.68°$ and $\theta_d = 5.95°$, guiding the ESG configuration to balance current collection and resolution needs.

Another design consideration for the deflection plates is the reduction of their size relative to the spacing between them. The capacitance of each leg of the deflection gate includes the stray capacitance between the electrode and the ground plates, C_s, plus half the capacitance between the electrodes, C_e. This results from the electrodes being biased to the same voltage but with opposite polarities, creating a virtual ground between them:

$$C_g = C_s + \frac{1}{2}C_e = \frac{2\varepsilon_0 h_g w_g}{s_p} + \frac{\varepsilon_0 t_g w_g}{2s_g} \tag{5}$$

where ε_0 is the absolute permittivity, h_g is the height of the plates, w_g is the width of the plates, and s_p is the spacing between ground and electrode plates. In addition, the total capacitance seen by each polarity of the HVPG must include the capacitance of the coaxial cable, leading to a total capacitance $C = C_g + C_{\mathrm{coax}}$. Commonly, coaxial cables have a capacitance of 100 pF/m. Using Eq.5, and taking into account a total of 1.5 meters of coaxial cable (air-side + vacuum), the setup employed had a total capacitance for each leg of approximately 300 pF. Note the importance of considering the cable capacitance, as in our case it corresponds to half of the total capacitance.

The last geometric consideration is that the aperture diameter should be such that the gate angle (angle between thruster emitter and gate aperture) matches that of the collector calculated before, $s_g = 4r_c L_{\mathrm{e,g}}/L_{\mathrm{ToF}}$, where $L_{\mathrm{e,g}}$ is the extractor-gate axial distance.

B. Time-of-flight resolution

A critical parameter in the design of the HVPG electronics is to achieve the desired time resolution for the ToF data. The required time resolution, Δt, in mass spectromentry for electrospray thrusters is calculated according to[12]

$$\Delta t = \frac{\Delta e}{2}t = \frac{\Delta e L_{\mathrm{ToF}}}{2v_i} \tag{6}$$

where Δe is the required energy resolution and t the flight time of an ion. Previous study has suggested that the required energy resolution to resolve all present species in an electrospray plume should be at least 5%[4]. Considering the most restrictive scenario with the minimum calculated L_{ToF} and the maximum velocity of EMI^+ ions (112 Dalton) at the highest

applied voltage, the ion flight time is approximately 7.4 μs. Consequently, using Eq.6 the minimum time resolution is estimated to be 180 ns. This time resolution is assumed to be the upper limit constraint of the required rise/fall times of the designed HVPG.

It is important to take into account the minimum current that the ToF setup is able to detect. Apart from the geometric constraint, the transimpedance amplifier (TIA) used plays a big role. In this work, the commercial TIA DHCPA-100 is used, which features high amplification (10^6) and high bandwidth (1.8 MHz). With this characteristics our setup is able to detect collected currents down to 10 nA. While working with an array of electrospray these currents are easily obtained, but while working with single emitters, which emit currents in the order of 100-200 nA[2,13,14], the collected currents can be lower, and other devices such as einzel lens to focus the beam or channeltrons can be used to enhance the collected current output[15].

III. ARCHITECTURE OF THE HIGH-VOLTAGE PULSE GENERATOR

The high-voltage pulse generators are classified in literature into two primary categories: classical generators and solid-state generators[16].

The HV pulses in classical generators are achieved by charging a group of capacitors in parallel and subsequently discharging them in series[17], and can be subdivided into the Magnetic Pulse Compressor (MPC), the Pulse Forming Network (PFN), the Multi-stage Blumlein Lines (MBL), and the Marx generator[18].

Actual power electronics switches can tolerate HV and deliver rapid on/off switching performance for narrow HV pulse generation, introducing several solid-state HVPGs. Some power electronics-based PGs emulate classical PGs, as the Marx generator. Furthermore, solid-state HVPGs exhibit a modular design, offering advantages as redundancy, scalability, and robust operation as well as being a long-lasting, and cost-effective alternative for pulse generation[18]. The use of solid-state switches into pulsed power supplies results in a smaller and more efficient system, leveraging power electronics control techniques[18] by the ease of gate control, snubberless operation, and reduced power losses. Power electronics-based PGs are based on DC-DC converters and can be categorized into three main groups based on their structure: Modular Multilevel Converter (MMC) based, non-MMC-based, and hybrid topologies[19].

The PG proposed is based on a bipolar non-MMC-based converter, where Capacitor-Diode Voltage Multipliers (CD-VMs) are used to achieve a high output-input voltage gain from a 5V DC supply, V_{in}, within a converter's duty cycle ranging from 0 to 50 %, with switching frequency below 200 kHz, making it suitable for in-house applications, and providing configurable regulated output voltages. However, the proposed PG requires for HV controlled switches at the output stage to modulate the generated HV DC voltage[17].

The architecture of the HV pulse generator is illustrated in Fig.3. It comprises three distinct subcircuits. Firstly, the HV-DC/DC converter generates bipolar HV rails from the 5V power bus while minimizing power conversion losses (therefore, heat dissipation). Subsequently, the bipolar kilovolt pulser circuit is connected in series with the ESG to modulate the generated HV DC. This subcircuit is driven by the fast pulsing low voltage logic, guaranteeing a swift rectangular pulse shape and simultaneous firing of both polarities to preserve the synchronized reflection times of the ESG.

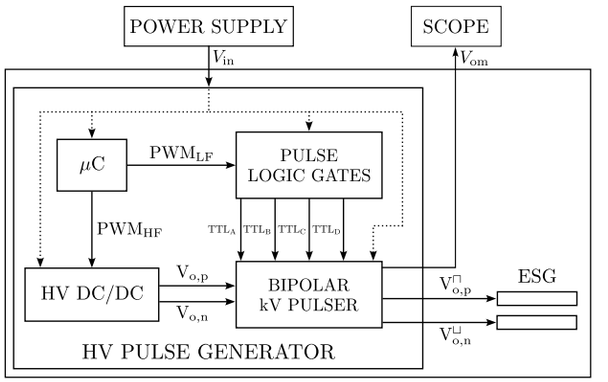

FIG. 3: HVPG: block diagram.

The HVPG presented in this study consumes a total power of 0.6 W in the most demanding scenario of supplying ± 1 kV. The electrical power required to operate each electrostatic gate, as calculated with Eq.7, is approximately 7.5 mW. This relatively low power consumption is attributed to the low pulse frequency, f_{PWM}, of around 25 Hz.

$$P_g = V^2 f_{\text{PWM}} \frac{C}{2} \tag{7}$$

A. HV DC/DC converter

The chosen topology for generating the bipolar HV outputs is the Forward-Flyback with two fifth-order Cockcroft-Walton Voltage Multiplier converter (FF-CW) in Discontinuous Conduction Mode (DCM) depicted in Fig.4[20]. The low-voltage NMOS MOSFET (n-Channel Metal Oxide Semiconductor Field Effect Transistor) switch, S_1, is controlled by a high-frequency Pulse Width Modulated (PWM) signal. Parasitic capacitance influence the circuit operation, particularly at high voltages and low power conditions, allowing quasi-ZVS (Zero Voltage Switching) to reduce energy losses[21].

This topology includes along the MOSFET output capacitance. C_{oss}, and diode junction capacitance, C_d, the transformer parasitic components. Eq.4 includes leakage inductance, L_{lk}, total winding parasitic capacitance, C_w, equivalent stray capacitance, C_{st}, and magnetizing inductance, L_m. To achieve quasi-ZVS is necessary to turn ON the MOSFET when the voltage across all parasitic capacitance has reached the minimum voltage levels in the resonance. This allows the resonant energy to flow through the parasitic capacitance and magnetizing inductance and to be conserved.

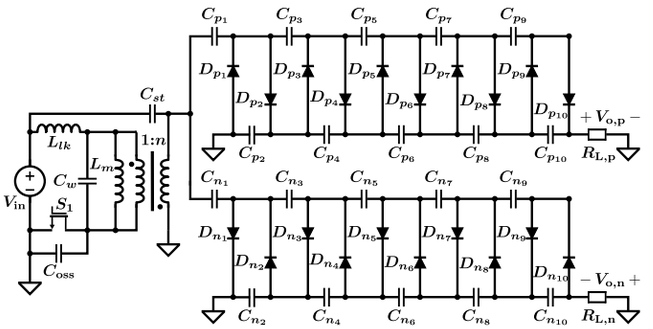

FIG. 4: Forward-Flyback converter with two fifth-order CW-VMR considering the transformer non-idealities.

Besides, the voltage drop in the CW-VMRs affects voltage gain since current passes through the CW-VMR capacitors before supplying energy to the load to charge them. Consecutive capacitors (even ones) partially discharge when delivering energy to the load and charging the opposite capacitor branch (odd ones), leading to an undesired output voltage drop. The total voltage gain considering the voltage drop effects can be expressed as shown in Eq.8, which depend on the number of voltage multiplier stages, m, transformer's turn ratio, n, switch-on fraction of the period, D_1, magnetizing inductance, switching frequency, f_{sw}, output capacitance, $C_{p_i} = C_{n_i} = C_o$), and equivalent output resistance, $R_L = R_{\mathrm{L,p}} || R_{\mathrm{L,n}}$. It is also assumed that $V_o \approx V_{\mathrm{o,p}} \approx |V_{\mathrm{o,n}}|$.

$$\frac{V_o}{V_{\mathrm{in}}} = \frac{\frac{nm}{2}\left[1+\sqrt{1+\frac{2R_L}{L_m f_{sw}}\left(\frac{D_1}{nm}\right)^2}\right]}{1+\frac{2m^3+3m^2+m}{12R_L f_{sw} C_o}} \tag{8}$$

From Eq.8, D_1 can be calculated according to Eq.9. Therefore, for a fix f_{sw}, tuning D_1 allows to vary the voltage applied to the ToF gate. The quasi-ZVS operation point can be achieved if f_{sw} is also tuned together with D_1.

$$D_1 = \frac{nm}{2}\sqrt{\frac{2L_m f_{sw}}{R_L}\left(\left[\frac{2V_o}{nmV_{\mathrm{in}}}\left(1+\frac{2m^3+3m^2+m}{12R_L f_{sw} C_o}\right)-1\right]^2-1\right)} \tag{9}$$

B. Bipolar kilovolt pulser

The HV DC signals are modulated into two rectangular waveforms, positive $V_{\mathrm{o,p}}^{\sqcap}$ and negative $V_{\mathrm{o,n}}^{\sqcup}$ with an oscillating frequency in the tens of hertz range, using the circuit depicted in Fig.5[22]. A pair of n-channel MOSFET switches in half-bridge configuration (HB), Single Pole Double Throw (SPDT) switches, are employed to alternate the connection of the output between ground and the HV DC source in each polarity to generate the pulses. Due to the high impedance nature of the time-of-flight gate and the presence of numerous capacitors in the CDVMs, the application of pulses does not induce a drop in the output voltage.

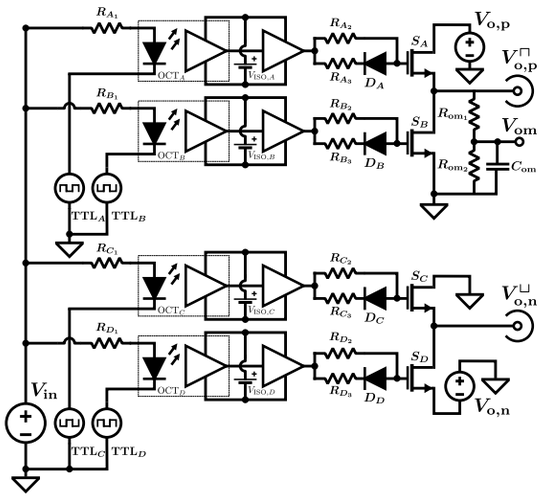

FIG. 5: Bipolar kilovolt pulser: schematic.

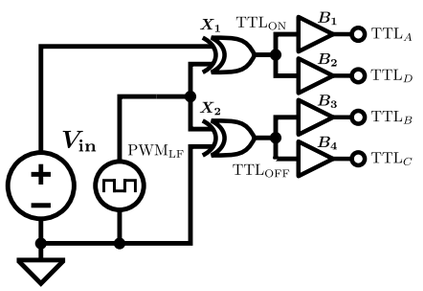

FIG. 6: Pulse forming logic: schematic.

The MOSFETs (S_A-S_B for the positive leg, S_C-S_D for the negative) are high side driven, creating floating gate-source voltages V_{GS} by using auxiliary isolated low-voltage supplies, V_{ISO}. These signals are generated from fast TTL logic-level inputs, described in Sec. III C, using an isolated high-speed octocoupler and a high-speed driver. Despite the logic provides transitions within tens of nanoseconds of rising and falling times, the primary delay of the PG arises from primarily the MOSFET and driver combination, imposing delay times of hundreds of nanoseconds.

To enhance turn-off speed, the output switches incorporate small series gate resistors, $R_{A-D_{2,3}}$, in parallel with Schottky diodes, D_{A-D}. The gate-source resistors prevents switch conduction if high voltage is applied before the isolated driving DC supplies are activated. The complete isolation of both drivers and their respective floating supplies allows a straightforward reversal of polarity. This reversal is achieved by simply switching the terminal of the high-voltage supply connected to ground. However, one of the limiting factors of HV MOSFETS pulse is the maximum switching voltage ($V_{\mathrm{DS,max}}$) which is half of the absolute rating provided by the manufacturer in the half-bridge configuration, $|V_{\mathrm{o,max}}| < |V_{\mathrm{DS,max}}/2|$.

An output monitor has been incorporated at the output of the positive HB. This monitor consists of a resistor divider, comprising a precision high-voltage resistor, $R_{\mathrm{om_2}}$, and a compensation capacitor in parallel, C_{om}. This configuration is designed to compensate for the stray shunt capacitance of the upper resistor, $R_{\mathrm{om_1}}$, ensuring the preservation of fidelity in the rapid timescales of the pulse waveform of resulting scoped low-voltage waveform, V_{om}.

C. Pulse forming logic

The TTL signals preceding the high-speed optocouplers are generated by means of the low-frequency pulse width modulation, $\mathrm{PWM_{LF}}$. A pair of XOR gates, $X_{1,2}$, generate the true and inverter input signals, $\mathrm{TTL_{ON}}$ and $\mathrm{TTL_{OFF}}$, and are integrated in the same chip, allowing to match the delay of the signals and to create a non-overlap interval to avoid output short-circuit condition. Subsequently, the signals are duplicated by means of logic buffers, B_{1-4}, to provide the ON and the OFF signal to each half bridge.

D. Operation Intervals

There are eight operation intervals considering the signals propagation delays, as shown in Fig.7:

- **Interval 1.** (t_0 **to** t_1): At time t_1, the $\mathrm{PWM_{LF}}$ transitions to the ON state, introducing a propagation delay between the rising edge of $\mathrm{PWM_{LF}}$ and the falling edge of $\mathrm{TTL_{OFF}}$.
- **Interval 2.** (t_1 **to** t_2): The safety delay is implemented between the falling edge of $\mathrm{TTL_{OFF}}$ and the rising edge of $\mathrm{TTL_{ON}}$ to prevent any overlapping conditions.
- **Interval 3.** (t_2 **to** t_3): The HBs are switched, producing a delay in the rising time of the HV pulse until it reaches HV DC levels, at which point the HV pulse becomes active.
- **Interval 5.** (t_3 **to** t_4): The HV pulse attains HV DC levels while in the ON state until t_6, influenced by the propagation delays.
- **Interval 6.** (t_4 **to** t_5): At time t_4, the $\mathrm{PWM_{LF}}$ transitions to the ON state, introducing a propagation delay between the falling edge of $\mathrm{PWM_{LF}}$ and the falling edge of $\mathrm{TTL_{ON}}$.
- **Interval 7.** (t_5 **to** t_6): The safety delay is implemented between the falling edge of $\mathrm{TTL_{ON}}$ and the rising edge of $\mathrm{TTL_{OFF}}$ to prevent any overlapping conditions.
- **Interval 8.** (t_6 **to** t_7): There is a falling time delay in the HV pulse until it reaches ground levels, at which point the HV pulse transitions to the OFF state.

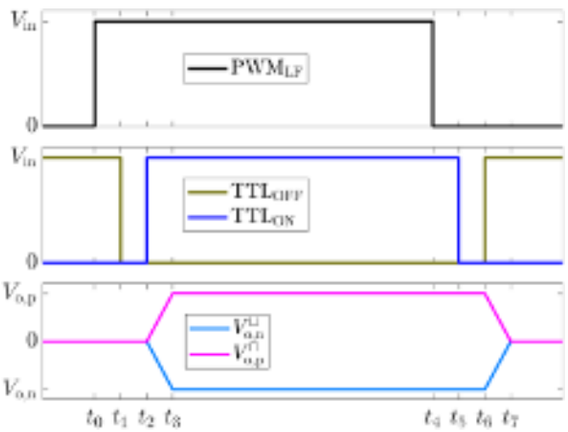

FIG. 7: Theoretical pulses waveforms showing $\mathrm{PWM_{LF}}$ in first plot, $\mathrm{TTL_{OFF}}$ and $\mathrm{TTL_{ON}}$ in second plot, and $V_{\mathrm{o,p}}^{\sqcap}$ and $V_{\mathrm{o,n}}^{\sqcup}$ in the third plot.

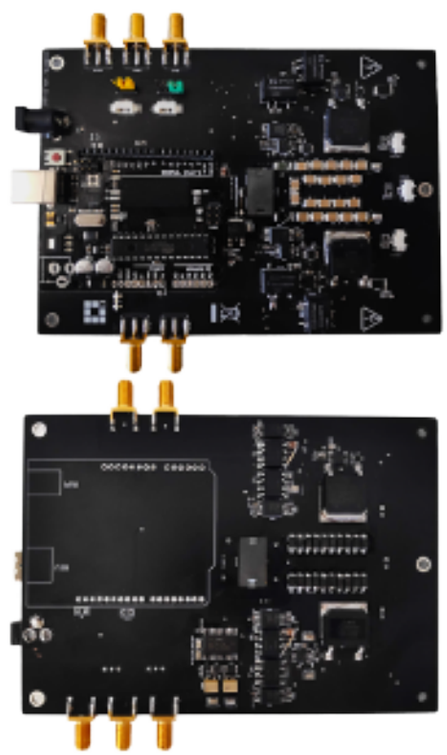

FIG. 8: Top and bottom view of the HVPG PCB.

IV. EXPERIMENTAL VERIFICATION

The experimental setup of the HVPG is depicted in Fig.8. The main components of the HV-DC/DC are summarized in Table I, where for the EI18 transformer, the E core part reference is given. For the HV pulser, IXYS IXTT1N200P3HV MOSFETs and high speed TC4422 drivers were employed, along with 6N137 optocouplers. The input pulse $\mathrm{PWM_{LF}}$ is originated from the ATMEGA328 microcontroller embedded in the Arduino. Both the duty cycle and the frequency of the high-voltage pulse can be specified. For the verification, a 1.25% duty cycle and 25 Hz frequency are selected.

TABLE I: High-voltage DC/DC components reference

Component	Identifier	Reference
MOSFET	S_1	IRFR7446TRPBF
Diodes	$D_{p_1}-D_{p_{10}}$ $D_{n_1}-D_{n_{10}}$	BYG23M
Capacitors	$C_{p_1}-C_{p_{10}}$ $C_{n_1}-C_{n_{10}}$	GCJ43DR7LV224KW01K
EI18 Transformer	-	B66283G0000X197

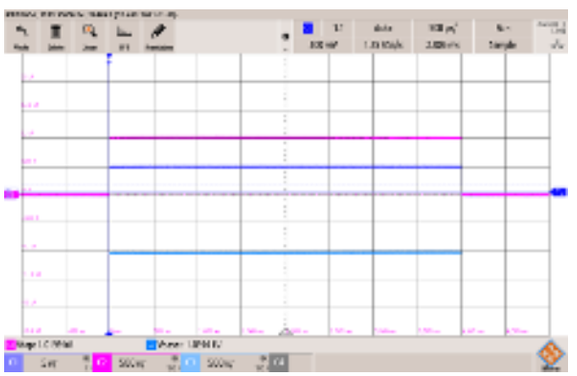

FIG. 9: Experimental pulse waveforms $\mathrm{PWM_{LF}}$, $V_{\mathrm{o,p}}^{\sqcap}$, and $V_{\mathrm{o,n}}^{\sqcup}$

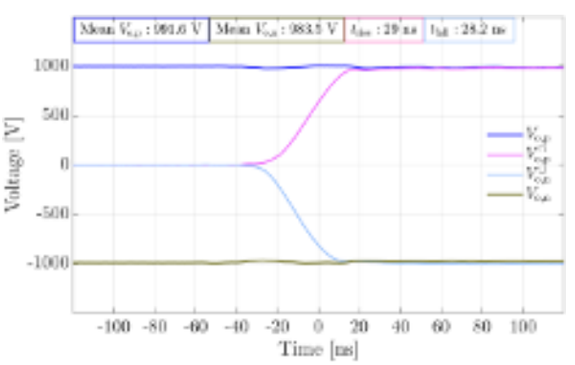

FIG. 10: Close-up image of rising edge.

To test the HVPG PCB, the high-voltage outputs were connected to the gate electrodes via a coaxial SHV (Safe high voltage) connector. This connection ensures that the casing of the coaxial SHV grounds the HVPG to the vacuum chamber when connected through the feed-through. Figure 9 illustrates the experimental $\mathrm{PWM_{LF}}$ input signal and the high voltage pulse signals $V_{\mathrm{o,p}}^{\sqcap}$ and $V_{\mathrm{o,n}}^{\sqcup}$, as directly obtained from the oscilloscope. Fig.10 and Fig.11 provide a detailed view of the rising and falling edges, constructed using exported data. Additionally, the experimental high-voltage DC/DC outputs, $V_{\mathrm{o,p}}$ and $V_{\mathrm{o,n}}$, are presented. The high voltage pulse signals exhibit clean rising and falling edges, with ringing and ripple in the range of 10-20 V, which is negligible as it corresponds to approximately 1% of the operating voltage. The oscilloscope used in this work is the Rohde&Schwarz RTB2004 (100MHz - 2.5GSa/s).

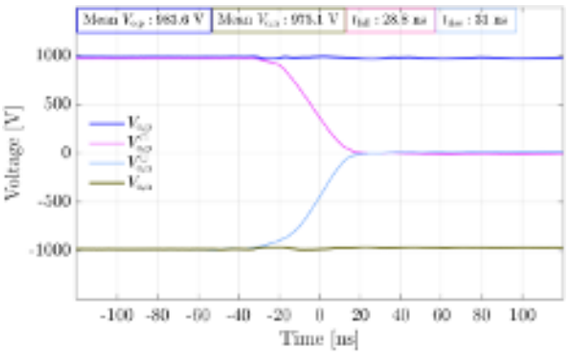

FIG. 11: Close-up image of falling edge.

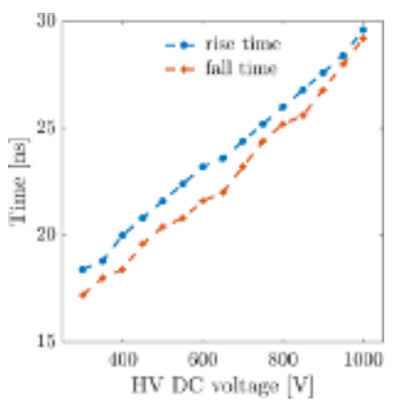

FIG. 12: Averaged rise and fall times of the pulse generator for different voltages.

The results of the HVPG comply with the estimated requirements, reaching the output voltage without voltage drop and with rise/fall in the vicinity of 30 ns, times much smaller than the requirement of 180 ns. With the selected $L_{\mathrm{ToF}} = 700$ mm, according to Eq.6 the energy resolution of the setup is 0.5%. ten times smaller than the one suggested by the literature[4]. Furthermore, the pulse generator underwent testing across various voltage settings, demonstrating consistent small rise and fall times for pulses ranging from 300 V to 1000 V. Fig.12 shows how the averaged rise/fall times linearly in-

crease with voltage, but remain below 30 ns for the nominal working voltage of 1 kV.

A. Time-of-flight measurements with an electrospray thruster

To completely verify the design, the pulse generator was tested in a real application with an electrospray thruster. An schematic of the geometrical parameters of the device employed is shown in Fig.13. It consists of an externally wetted electrospray thruster featuring 101 cones distributed in an hexagonal packaging with 900 μm spacing, 180 μm height and 30° half-angle, compacting them to an active area of 1 cm^2, a 110 μm tip-to-extractor distance, and a 450 μm extractor holes diameter. The propellant employed is the aforementioned EMI-BF_4, and the operating voltage is set to $\pm$1600 V.

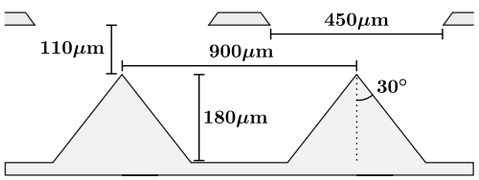

FIG. 13: Externally wetted electrospray schematic with the geometrical parameters of the thruster prototype.

To validate the ToF setup for characterizing thruster performance, several limitations must be considered. One significant limitation is the divergence of electrospray arrays due to dispersion forces[23,24], which can reach angles of 40-50°[25–27]. This divergence implies that the linear ToF configuration can only assess the central performance of the thruster. Additionally, for externally wetted electrosprays, the passive flow control prevents the mass flow rate obtained from ToF measurements from being directly correlated with the actual mass flow rate, unlike in systems with capillary emitters. Nevertheless, the functionality of the HVPG is confirmed, as it effectively drives the electrostatic gate to deflect incoming particles, achieving the primary objective of this study .

The thruster operates using a square pulse that alternates polarities every second, facilitating emission of both positive and negative particles. Synchronization of gate pulses with the flat part of the applied voltage to the thruster is achieved through the HVPG, which offers two methods: utilizing dedicated software to control pulsing via microcontroller PWMs or employing an external pulse generator. In our study, we opt for the microcontroller-driven approach facilitated by our software, which synchronizes both the HVPG and the thruster's HV amplifier. This synchronization is pivotal during polarity switching to maintain standard operation and ensure accurate experimental measurements.

Given the pulse frequency of 25 Hz, approximately 20 measurements are obtained during each polarity cycle. This slightly reduced number ensures data collection occurs within the stable operation phase of the thruster. The emission characteristics of the thruster reveal consistent operation, with

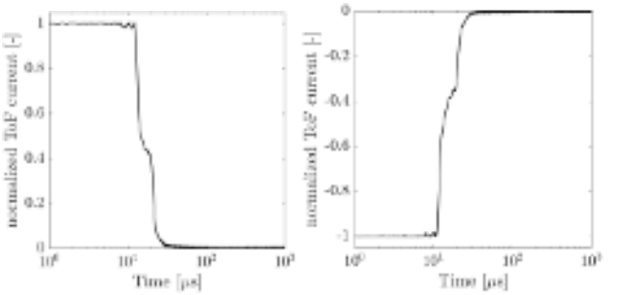

FIG. 14: Time-of-flight normalized collected current for negative emission versus time.

emission currents measured at 178 μA during the positive polarity and 115 μA during the negative polarity. For a more comprehensive understanding of the thruster's operational specifics in this experiment, detailed information can be found in[28].

ToF data is presented separately for positive and negative emission cases, as the composition of particles in each plume differs. In Fig.14, normalized time-of-flight current data is depicted. To mitigate random noise, the displayed traces result from averaging 200 ToF measurements. Analysis of the data reveals two distinct steps, corresponding to the flight times of single ion particles and molecules with one degree of solvation. For a clearer estimation of the particles, charge-to-mass spectra are constructed in Fig.15 and Fig.16. Known oligomers with discrete values of charge and mass manifest as peaks in the spectra, with a predominance of EMI^+ and BF_4^- species in the plume. This is followed by oligomers with one degree of solvation, such as EMI^+(EMI-BF_4) and BF_4^-(EMI-BF_4), and a smaller fraction of more highly solvated molecules. Droplets, if present, would appear as a distribution in the spectra; however, they are not observed in this plume. This condition is referred to as the pure ionic regime[29], characterized by the presence of distinct ion molecules. From a propulsion perspective, this regime enhances propulsive performance efficiency.

The low rise/fall times of the HVPG allow for the observation of molecules resulting from fragmentation[12], occurring between the known particles. Such molecules form when accelerated molecules break down into their constituent particles.

V. CONCLUSIONS

The paper introduces a novel bipolar high-voltage pulse generator tailored for application in electrospray thrusters time-of-flight mass spectrometry. This proposed generator relies on a bipolar high-gain converter, specifically the Forward-Flyback with Cockcroft-Walton voltage multiplier, which operates from a 5V DC supply. The generator modulates HV rails into pulses through a bipolar kilovolt pulser composed of high voltage MOSFETs and high-speed driving circuitry. This modulation is accomplished without inducing voltage drop in

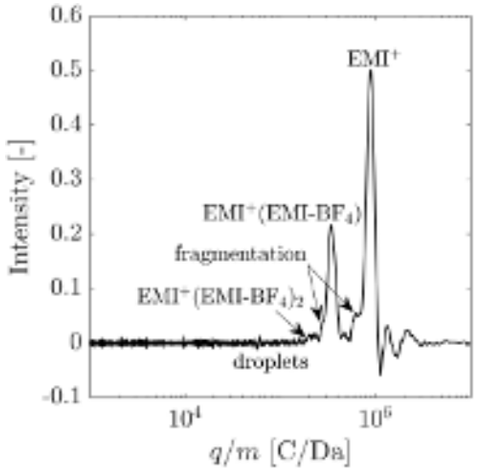

FIG. 15: Time-of-flight charge-to-mass spectra for positive emission

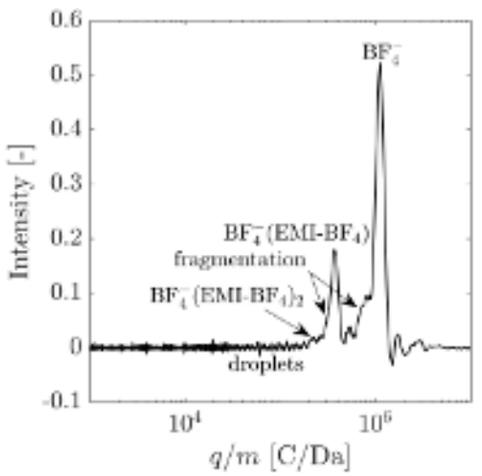

FIG. 16: Time-of-flight charge-to-mass spectra for negative emission

the high voltage rails.

The bipolar pulses are synchronized, with a non-overlap interval strategically integrated to avert short-circuit conditions in the pulse forming logic. Experimental validation of the pulse generator corroborates theoretical descriptions, showcasing configurable pulse amplitudes and fast rising and falling pulse times of 30 ns at 1 kV. which constitute the worst case scenario.

Primarily designed to drive the electrostatic shutter gate of a time-of-flight mass spectrometer, this generator proves well-suited for investigating the plume composition of electrospray sources. An experimental characterization of an electrospray thruster has shown the ability of clearly distinguish all the particles present in the plume, including particles formed by fragmentation.

ACKNOWLEDGMENTS

This work was supported by the “Comunidad de Madrid" under “Ayudas destinadas a la realización de doctorados industriales" program IND2020/TIC-17316.

DATA AVAILABILITY STATEMENT

The data that support the findings of this study are available from the corresponding author upon reasonable request.

[1]P. Lozano and M. Martinez-Sanchez, “Efficiency estimation of emi-bf4 ionic liquid electrospray thrusters,” in *41st AIAA/ASME/SAE/ASEE Joint Propulsion Conference & Exhibit* (2005) p. 4388.
[2]P. Lozano and M. Martinez-Sanchez, “Ionic liquid ion sources: characterization of externally wetted emitters,” Journal of colloid and interface science **282**, 415–421 (2005).
[3]J. F. De La Mora and I. G. Loscertales, “The current emitted by highly conducting taylor cones,” Journal of fluid mechanics **260**, 155–184 (1994).
[4]P. C. Lozano, “Energy properties of an emi-im ionic liquid ion source,” Journal of Physics D: Applied Physics **39**, 126 (2005).
[5]M. Gamero-Castaño and A. Cisquella-Serra, “Electrosprays of highly conducting liquids: A study of droplet and ion emission based on retarding potential and time-of-flight spectrometry,” Physical Review Fluids **6**, 013701 (2021).
[6]D. Villegas-Prados, J. Cruz, M. Wijnen, S. Correyero, P. Fajardo, and J. Navarro-Cavallé, “Impact of propellant temperature on the emission regime of an externally wetted electrospray system using time-of-flight mass spectrometry,” Acta Astronautica **213**, 145–155 (2023).
[7]K. W. Jung, S. S. Choi, and K.-H. Jung, “An electron-impact ionization time-of-flight mass spectrometer using a simple high-voltage square pulse generator,” Review of scientific instruments **62**, 2125–2130 (1991).
[8]P. Marmillod, S. Antonioni, and U. J. Lorenz, “A radio frequency/high voltage pulse generator for the operation of a planar multipole ion trap/time-of-flight mass spectrometer,” Review of Scientific Instruments **84** (2013).
[9]J. Kim, “Construction and test of an ion-gate with high-voltage switch system for single-reflection time of flight measurement,” AIP Advances **10** (2020).
[10]O. K. Yoon, I. A. Zuleta, M. D. Robbins, G. K. Barbula, and R. N. Zare, “Simple template-based method to produce bradbury-nielsen gates,” Journal of the American Society for Mass Spectrometry **18**, 1901–1908 (2007).
[11]L. J. Perez-Lorenzo and J. F. de la Mora, “Probing electrically driven nanojets by energy and mass analysis in vacuo,” Journal of Fluid Mechanics **931**, A4 (2022).
[12]C. E. Miller, *Characterization of ion cluster fragmentation in ionic liquid ion sources*, Ph.D. thesis, Massachusetts Institute of Technology (2019).
[13]B. Ticknor, S. Miller, and Y.-H. Chiu, “Mass spectrometric analysis of the electrospray plume from an externally wetted tungsten ribbon emitter,” in *45th AIAA/ASME/SAE/ASEE Joint Propulsion Conference & Exhibit* (2009) p. 5088.
[14]Y.-H. Chiu, G. Gaeta, T. Heine, R. Dressler, and D. Levandier, “Analysis of the electrospray plume from the emi-im propellant externally wetted on a tungsten needle,” in *42nd AIAA/ASME/SAE/ASEE Joint Propulsion Conference & Exhibit* (2006) p. 5010.
[15]P. C. Lozano-Tovar, *Studies on the ion-droplet mixed regime in colloid thrusters*, Ph.D. thesis, Massachusetts Institute of Technology (2003).
[16]A. Elserougi, A. M. Massoud, A. Ibrahim, and S. Ahmed, “A high voltage pulse-generator based on dc-to-dc converters and capacitor-diode voltage multipliers for water treatment applications,” IEEE Transactions on Dielectrics and Electrical Insulation **22**, 3290–3298 (2015).
[17]J. Mankowski and M. Kristiansen, “A review of short pulse generator technology,” IEEE Transactions on Plasma Science **28**, 102–108 (2000).
[18]M. R. Q. R. Abadi, M. H. Marzebali, V. Abolghasemi, and M. H. Anisi, “High-voltage pulse generators for electroporation applications: A systematic review,” IEEE Access **10**, 64933–64951 (2022).
[19]M. A. Elgenedy, “High-voltage pulse generators incorporating modular multilevel converter sub-modules,” (2018).

[20]F. Blázquez-Plaza, A. Barrado, and M. Wijnen, "Power converter with high gain, high performance for space thrusters based on electrospray technology," in *Aerospace Europe Conference EUCASS-CEAS* (2023).
[21]J. A. Serrano, P. Alou, and J. A. Oliver, "Dcm forward-flyback converter with cockcroft-walton voltage multiplier: steady-state analysis considering the influence of the parasitic capacitances at very low power and very high voltage gain," in *2019 IEEE Energy Conversion Congress and Exposition (ECCE)* (IEEE, 2019) pp. 6841–6847.
[22]P. Horowitz and W. Hill, *The art of electronics* (Cambridge university press Cambridge, 1978).
[23]M. J. Breddan and R. E. Wirz, "Electrospray plume divergence: Background pressure influence," Journal of Aerosol Science , 106417 (2024).
[24]M. Gamero-Castaño and M. Galobardes-Esteban, "Electrospray propulsion: Modeling of the beams of droplets and ions of highly conducting propellants," Journal of Applied Physics **131** (2022).
[25]F. A. Hill, E. V. Heubel, P. P. de Leon, and L. F. Velásquez-García, "High-throughput ionic liquid ion sources using arrays of microfabricated electrospray emitters with integrated extractor grid and carbon nanotube flow control structures," Journal of Microelectromechanical Systems **23**, 1237–1248 (2014).
[26]E. Petro, A. Bruno, P. Lozano, L. E. Perna, and D. Freeman, "Characterization of the tile electrospray emitters," in *Aiaa propulsion and energy 2020 forum* (2020) p. 3612.
[27]G. Yuntao, S. Wei, S. Zhenning, W. Zhiwen, H. Jianwu, Y. Chao, and W. Ningfei, "Direct thrust test and asymmetric performance of porous ionic liquid electrospray thruster," Chinese Journal of Aeronautics **36**, 120–133 (2023).
[28]D. Villegas-Prados, J. Cruz, M. Wijnen, P. Fajardo, and J. Navarro-Cavallé, "Emission and performance characterization of ionic liquids for an externally wetted electrospray thruster," Acta Astronautica (2024).
[29]I. Romero-Sanz, R. Bocanegra, J. Fernandez De La Mora, and M. Gamero-Castaño, "Source of heavy molecular ions based on taylor cones of ionic liquids operating in the pure ion evaporation regime," Journal of Applied Physics **94**, 3599–3605 (2003).